Master Thesis

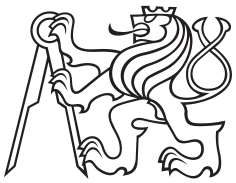

Czech Technical University in Prague

F3

Faculty of Electrical Engineering
Department of electromagnetic field

Fiber-optic Based Fabry-Perot interferometry for High-resolution Motion Detection

Shou-Yue Chen

Supervisor: Ing. Matěj Komanec, Ph.D.
Co-supervisor: Ing. Tomáš Němeček, Ph.D.
May 2020

Acknowledgements

I am grateful to Ing. Matěj Komanec, Ph.D (komanmat@fel.cvut.cz) and Ing. Tomáš Němeček, Ph.D (nemect10@fel.cvut.cz) for their guidance. This thesis would have not been possible without their contribution. I would like to thank all colleagues who contributed to this study including Dmytro, Peter, and Daniel. Thanks to Tomáš for helping in the data collection and analysis, teaching how to access data and comments on the draft of the thesis. The quality of the experiments was greatly enhanced by the gracious assistance of prof. Ing. Stanislav Zvánovec, Ph.D (xzvanove@fel.cvut.cz). Thanks to Matěj for advicing on the whole thesis design. Thanks to Prof. San-Liang Lee for strong support in the double-degree program. This research has been supported by the Wireless and Fiber Optics group of the Department of electromagnetic field of the Czech Technical University in Prague and the Optical Fiber Network Lab of National Taiwan University of Science and Technology.

Declaration

I declare that this work is all my own work and I have cited all sources I have used in the bibliography.

Prague, May , 2020

Abstract

I propose and demonstrate a highly-sensitive motion detection based on fiber Fabry-Perot interferometry with resolution below 100 nm. The interferometer is based on a fiber-optic collimator, specially designed for efficient signal back-coupling, and a discrete moving reflective mirror forming the Fabry-Perot cavity. To enhance the sensing range, I propose a dual-cavity fiber Fabry-Perot interferometer, the main idea based on the interference pattern of the two signals. Experimental results then showed that the proposed sensor is capable of sensing in a displacement range up to 1500 μm with resolution of 2 nm and stability within a wide area of 2 mm. Furthermore, I evaluated the influence of the angular offset on FFPI performance.

Keywords: Fabry-Perot Interferometer, Dual-cavity, motion detection, high resolution

Supervisor: Ing. Matěj Komanec, Ph.D.

Co-supervisor: Ing. Tomáš Němeček, Ph.D.

Acronym-list

FPI - Fabry-Perot interferometer
FFPI - fiber Fabry-Perot interferometer
SMF - single mode fiber
PC - physical contact
LS - laser source
ATT - attenuator
CIRC - circulator
M - mirror
PC - personal computer
PD - photodetector
OSC - oscilloscope
NA - numerical aperture
MFD - mode-field diameter
LED - Light-emitting diode

Contents

Figures

Chapter 1

Introduction

Fiber-optic sensing technology has attracted high interest in recent years due to its advantages such as immunity to electromagnetic interference, remote access, fast and real-time response, ease of fabrication and small size. Moreover, fiber-optic sensors provide extreme sensitivity and are capable of multiparameter detection, which is hard to achieve using traditional sensing approaches [1-2]. Fiber-optic sensors are widely applied in various fields, such as biology, chemistry, structural health monitoring, atomic resolution microscopy and vibration analysis. Physical parameters such as liquid level, liquid and gas concentration, strain, temperature, curvature, and displacement can be measured [2-5].

In particular, fiber-optic displacement sensors are important in industrial and scientific applications because of their high precision and wide operational range. Therefore, they are used for precise movement control and position monitoring [6]. Several types of fiber-optic displacement sensors have already been developed, primarily including wavelength modulated sensors, reflective intensity modulated sensors, and interferometric sensors [2]. Interferometric sensors can often be exploited due to excellent sensitivities and high resolution, and they are more stable than intensity-based sensors [2]. Fiber equivalents of the Mach-Zehnder and Michelson interferometers have been used and discussed in numerous applications for measuring dynamic strains, and temperature. Chen et al. [7] proposed a Mach-Zehnder Interferometer (MZI) displacement sensor by concatenating two core-offset joints with a measurement dynamic range of 1 mm. A Michelson Interferometer (MI) with a displacement measurement limit of 3 mm was proposed by Rong et al. [8]. However, both of these interferometers require an additional reference interferometer arm which has to be isolated from the measured parameter as well as from the measuring environment.

In 1897, French scientists C. Fabry and A. Perot invented a special interferometer [9-11]. This interferometer is known as the Fabry-Perot interferometer (FPI). During the 1980s, with the continuous advancement of silicon glass, optical fibers and fine processing technology, FPI was manufactured by using a simpler and more precise process [12]. Along with the improvement of the manufacturing process, the performance of FPI has also been greatly improved. In fiber Fabry-Perot interferometers (FFPIs), on the other hand,

only one arm is required for sensing, which leads to the reduction of sensor complexity [1]. FFPI enables greater flexibility in sensor configuration either as an intrinsic-type or an extrinsic-type device [1], and offers one of the simplest approaches to displacement sensing [6].

After the signal enters FFPI, multiple reflections are generated in the Fabry-Perot cavity which then form an interference pattern. There are several improved displacement detection methods using FFPI, such as the dual-cavity FFPI method was proposed in order to solve directional ambiguity [1]. Dual-cavity FPI also overcomes limitation in the sensing range (maximum displacement). Tapered-fiber method was applied with the work on long range displacement [6], extrinsic FFPI sensor was constructed to reach wide dynamic displacement range up to 2 cm and resolution of 0.27 μm [2].

In this thesis, I propose a simple FFPI displacement sensor setup for ultra-sensitive motion detection as well as a dual-cavity FFPI configuration. Resolution below 100 nm is acquired. First, I focus in Chapter 2 on the theoretical background of the basic Fabry-Perot interferometer, coherence length and coupling conditions, altogether with numerical aperture. Simulation of angular misalignment and beam propagation is then introduced in Chapter 3. Simple experimental setup is then shown in Chapter 4. Based on the proposed the FFPI working area, sensitivity, resolution and stability are observed and discussed in Chapter 5. Enhanced dual-cavity FFPI performance for different wavelengths is presented at the end of Chapter 5. Finally, in the Conclusion I summarize all the achieved results.

Chapter 2

Theoretical background

2.1 Fiber-based Fabry-Perot interferometer

The basic Fabry-Perot interferometer (FPI) is a multiple-beam interferometer [13]. In principle, FPI consists of two parallel planes, both having power reflectivity R, are separated by a distance d, as shown in Fig. 2.1. The gap between two planes can be varied by moving one of the mirrors. If a light beam is launched onto the mirror M1 at an incident angle α, a part of the light will penetrate through the left mirror and propagates to the right mirror M2 at point A. At this point, part of the light (T_1) will pass through the mirror and the other part will be reflected back to the left mirror at point B. This process will be repeated many times until the amplitude is significantly reduced due to the multiple reflection losses [17].

The phase delay is carried out by the traces difference between two mirror, also referred to path length difference which is given by

$$\Delta L = 2d\,cos\alpha \tag{2.1}$$

where d is the cavity length, α is incident angle of input light.

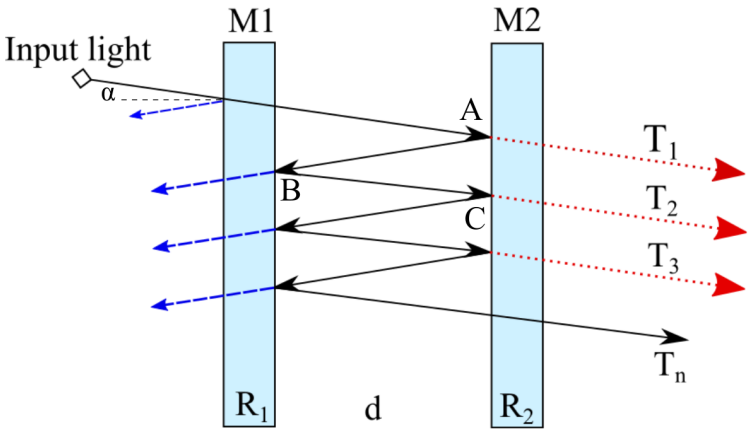

Figure 2.1: Illustration of Fabry-Perot interferometer with two mirrors separated by a distance d.

There are several key parameters to characterize the performance of FPI. The working area of FPI is defined by the linear section of interference pattern. In this area we can easily read out the dependence of displacement on the voltage change. This dependence is used for movement calibration. Using the calibration curve, the results in voltage can be converted into movement. The sensitivity of FPI sensor can be defined as the ratio of sensor response (in our case a voltage difference) and corresponding movement/displacement. Resolution is then derived from the sensitivity along with standard derivation which describes the measurement noise of the FPI sensor. The detail discussion will be present in Chapter 5.

In a fiber Fabry-Perot interferometer (FFPI) the cavity is formed by an optical fiber and a reflective surface. Resonance is established between the cavity and the input signal when the full round-trip cavity length is a multiple of the wavelength of the input signal.

Optical fibers are circular dielectric wave-guides that can transport optical signal. They have a central core surrounded by a concentric cladding with slightly lower (by $\approx 1\%$) refractive index as shown in Fig. 2.2.

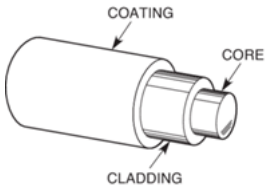

Figure 2.2: Cross section view of a fiber [14].

The principle of FFPI operation is based on the reflection from the fiber end-facet and the mirror, as shown in Fig. 2.3. Constructive interference occurs at the resonance, allowing the energy of the input light to penetrate out of the fiber and build up in amplitude inside the cavity, the cavity transmits the incident light with maximum power. Off resonance, destructive interference is generated, all the incident light is reflected back to the source and results minimum power at the output. The total construction interference is given by

$$I_{max} = I_1 + I_2 + 2\sqrt{I_1 I_2}\cos\delta, \delta = 0 \tag{2.2}$$

where I_1 and I_2 are the light intensities reflected from the mirror M and end-face of the fiber, respectively; δ is the phase difference arising from a combined path length and initial phase-angle difference [2]. On the other hand, the total destructive interference is expressed as

$$I_{min} = I_1 + I_2 - 2\sqrt{I_1 I_2}\cos\delta, \delta = \pi \tag{2.3}$$

in the case of total constructive interference, the phase difference between the two waves is an integer multiple of 2π, and the disturbances are in-phase. A minimum irradiance results when the waves are 180° out-of-phase and it is referred to as total destructive interference.

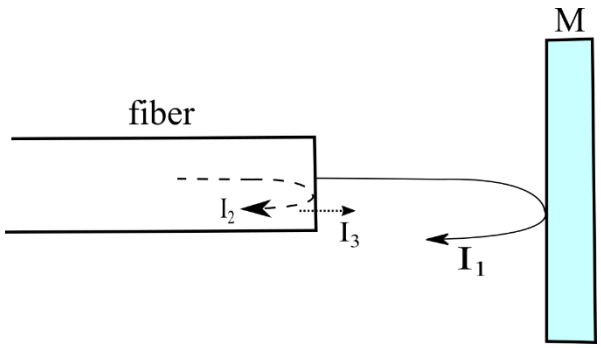

Figure 2.3: Simple scheme of a displacement sensor based on the Fabry-Perot interferometer. The cavity is formed between fiber end-facet and mirror **M**. I_1 and I_2 are reflected waves from the mirror and the fiber end-facet, I_3 is negligible noise signal in the system.

The FFPI sensor presented in this thesis exploits only the first order of reflected beam I_1 and the reflected beam I_2 at the fiber-air interface (fiber end-facet). Noise signal can be neglected since the intensity of the second reflection I_3 is relatively small, as shown in Fig. 2.3.

2.2 Coherence condition

Coherence is required for the interference phenomena to occur. There is temporal coherence and spatial coherence, the former one corresponds to monochromatic light source and later one means cross-correlation. The degree of coherence is often described by the coherence length parameter. One fundamental requirement for interference is that the two participating beams have to be mutually coherent. This requires that the path length difference between the two interferometer arms be shorter than the coherence length of the optical signal to be measured. It is measured by the change of cavity length from no interference to total constructive interference. Coherence length is determined by [18]

$$L = \sqrt{\frac{2\ln 2}{\pi}} \frac{\lambda^2}{n_{air}\Delta\lambda} = \sqrt{\frac{2\ln 2}{\pi}} \frac{c}{n_{air}\Delta f} \tag{2.4}$$

where $\Delta\lambda$ is linewidth of light source, n_{air} is refractive index of air. The longer coherence length is, the more monochromatic light source is. Interference phenomena is observed when two waves' path difference is less than coherence length. Laser has better temporal length of hundreds of meters, while LED is several hundred nanometers.

Coherence length is then restricted the distance that the mirror can scan in FFPI such that:

$$L_{scan} \ll \frac{c}{n\Delta f} \tag{2.5}$$

If the arm's-length difference is longer than the signal coherence length, the coherent interference will not happen and the detected signal will become a random function of time [17].

2.3 Fiber arm and end-facet back-reflection

In the designed FFPI sensor, signal propagating in the fiber which is then reflected at the fiber end-facet is referred as the first FFPI arm (the fiber arm); the path from the fiber to the the mirror and back to the fiber is referred to the second FFPI arm (the mirror arm, discussed in the next Section).

Back-reflection of the fiber end-facet is determined by the fiber end-facet preparation, i.e. angle and polishing. Depending on the ratio between the transmission and the reflection at the fiber end-facet, we can distinguish four fiber end-facet categories, such as flat polish, Physical Contact (PC) polish, Super PC (SPC) and Ultra PC (UPC) polish, and Angled PC (APC) polish. As shown in Fig. 2.4, a flat polish of the fiber end-facet will result in a back reflection of about -14 dB (4%, defined just by silica-air interface); PC have back reflections of -30 to -40 dB; SPC and UPC enhanced the surface quality and result in reflections of -40 to -55 dB; APC has back reflections of ≤ -60 dB and can routinely be accomplished with this type of polish [14].

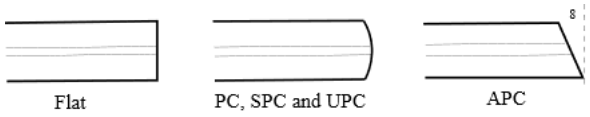

Figure 2.4: Fiber end-facet options.

Back reflection is also affected by losses in FFPI [17]. After each roundtrip in the FFPI cavity, the optical signal is reduced by efficiency η multipled by the mirror reflectivity R instead of just R, as shown simplified in Fig. 2.1. The extra loss factor η may be introduced by cavity material absorption and beam misalignment. The major cause of beam misalignment is that the two mirrors that form the FPI are not exactly parallel. As a consequence, after each roundtrip the beam exiting from FFPI only partially overlaps with the previously reflected beam; therefore the strength of the interference between them is reduced. For simplicity, we still use R to represent the FFPI mirror reflectivity; however, this is an effective reflectivity which includes the effect of cavity loss.

2.4 Mirror arm and back-coupling efficiency

In FFPI, the light beam launched out from fiber end-facet is reflected at the mirror **M** and coupled back into the fiber. The back-coupling efficiency is dependent on Numerical Aperture (NA) of the fiber and the mode-field diameter (MFD) overlap of the reflected light beam and the fiber intrinsic MFD. It is important to take into consideration both of these parameters as they are responsible for losses in FFPI.

The mode-field diameter can be calculated for a collimated beam. For calculations, the simpler case is a single-mode fiber. Here, MFD can be calculated with reasonably good accuracy using the following equation [15]

$$\omega_{collimated} = f \cdot \theta_{fiber} \approx f \cdot \frac{\lambda}{\pi \omega_{fiber}} \tag{2.6}$$

where θ_{fiber} is full acceptance angle of fiber and ω_{fiber} is beam waist. f is focal length of the fiber collimator. A smaller mode size of the fiber implies a larger beam divergence and leads to a larger collimated beam. In this thesis, a fiber collimator is used to gather light beam much more efficiently and reduced the loss of back reflection.

NA is defined as the sine of the largest angle an incident ray can have for total internal reflectance to occur in the fiber core. The full acceptance angle is 2α, and NA is defined as:

$$NA = \sin\alpha = \sqrt{n_1^2 - n_2^2} \tag{2.7}$$

where n_1 and n_2 are refractive index of core and cladding of the optical fiber. A higher core index, with respect to the cladding, means larger NA. NA of a fiber can be determined by measuring the divergence angle of the light cone, it emits when all its modes are excited. Qualitatively, NA is a measure of the light gathering ability of a fiber. It also indicates how easy it is to couple the reflected light beam into the fiber.

In the proposed FFPI sensor, because of the small numerical aperture (NA=0.12 at 1550 nm) of the single-mode fiber (SMF) [17], I employ a fiber collimator to increase the back-coupling efficiency. It is a conventional SMF spliced on a segment of graded-index multimode fiber with a 100 μm core diameter. The collimated beam has its waist located at approximately 300 μm from the fiber collimator. The basic principle is shown in Fig. 2.5. The power transfer function of FFPI using a fiber collimator can be expressed as [17]:

$$T_{FP}(\lambda) = \frac{(1-R)^2}{(1-R)^2 + 4R\sin^2(\frac{2\pi\, d\, n\cos\alpha}{\lambda})} \tag{2.8}$$

where R is reflectivity of mirror, d is cavity length, λ is wavelength of source. In the collimated case, incidence angle $\alpha = 0$, equation 2.8 can be simplified to:

$$T_{FP}(\lambda) = \frac{(1-R)^2}{(1-R)^2 + 4R\sin^2(\frac{2\pi\, d\, n}{\lambda})} \tag{2.9}$$

which indicates again that NA is an important factor when considering backward coupling in the mirror FFPI arm.

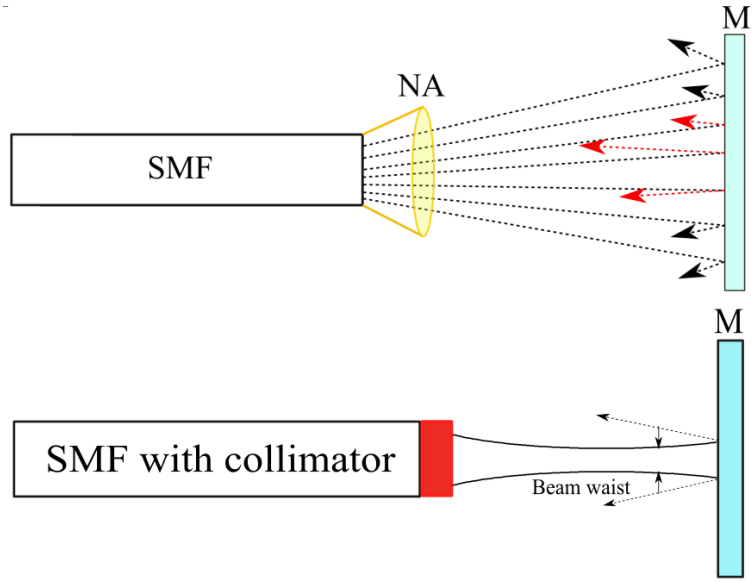

Figure 2.5: Illustration of a divergent and collimated beam propagation in the proposed FFPI.

Backward coupling is also affected by angle misalignment of the mirror since two parallel surfaces are required for optimal FFPI performance. It is necessary to ensure the fiber end and mirror are in perfect alignment [16]. If the mirror is tilted by an angel θ, non-parallelism causes large difference from theoretical predictions made for an ideal FFPI. As depicted in Fig. 2.6, the spatial frequency of transmitted beam components will gradually shift from input spatial frequency with increasing number of cavity reflections. In order to avoid misalignment of cavity, the mirror's angle alignment is an important preparation during the measurement which can be achieved by using a precise angular stage and manually obtain the maximum power output by power meter.

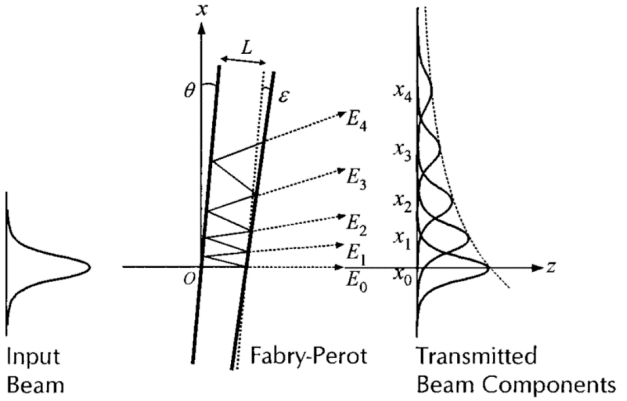

Figure 2.6: Optical geometry of a misaligned FPI [16].

2.5 Dual-cavity fiber Fabry-Perot interferometer

Dual-cavity FFPI exploits two fibers which form two cavities of a different length for the same mirror **M**. The purpose of this configuration change is to determine direction of motion and wider movement range by utilizing the working area of FPI cavities. Since the second working area of FPI is shifted, as shown in Fig. 2.6, two output interference pattern I_{FPI_1} and I_{FPI_2} can make use of the other's working area to overcome sensitivity limitation of output interference pattern. We can easily write the interference intensity as:

$$I_{FPI_1} = I_1 + I_2 + 2\sqrt{I_1 I_2}\cos\delta_1, \delta_1 = \frac{4\pi\, n\, L_1}{\lambda} \tag{2.10}$$

$$I_{FPI_2} = I_3 + I_4 + 2\sqrt{I_3 I_4}\cos\delta_2, \delta_2 = \frac{4\pi\, n\, L_2}{\lambda} \tag{2.11}$$

where I_1 and I_2 are respectively reflected by fiber 1 end-facet and mirror, I_3 and I_4 are light intensities from fiber 2; n is air refractive index, L_1 and L_2 are resonant cavity lengths; λ represents wavelength. By selecting different cavity length, we can observe wider sensing range compared to single cavity FPI which is discussed in Chapter 2.1.

In order to have quick and precise calculation, the only different parameter of two cavities is cavity length and all the rest of parameters such as source wavelength, fiber category should remain unchanged.

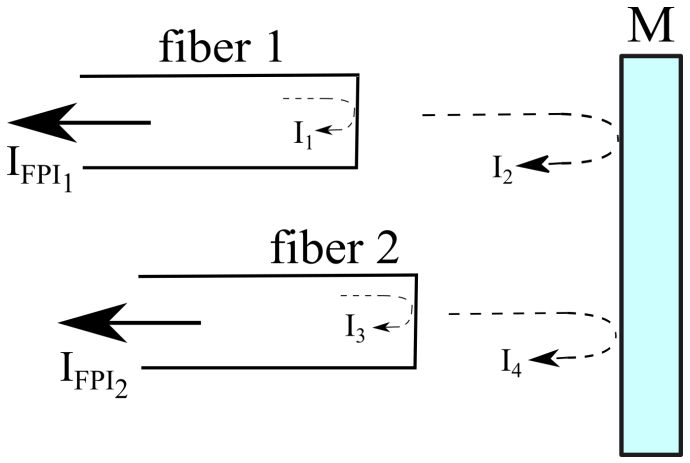

Figure 2.7: Scheme of a dual-cavity FFPI displacement sensor. Two cavities are formed between two fibers and one mirror **M**.

Chapter 3

FFPI simulation

3.1 Simulation of mirror angular misalignment

In this section I present a simulation of mirror angular misalignment. The simulation is carried out in ZEMAX in the non-sequential mode. I consider wavelength of 1550 nm (which corresponds to the following practical measurements), Gaussian beam source of 10 mW output optical power, a single-mode optical fiber and a 100 % reflective mirror. The mirror position is tilted and the fixed FFPI cavity length is 0.05 mm, as shown in Fig. 3.1. A detector and Gaussain beam source are placed at the input of the fiber, to detect the output interference image.

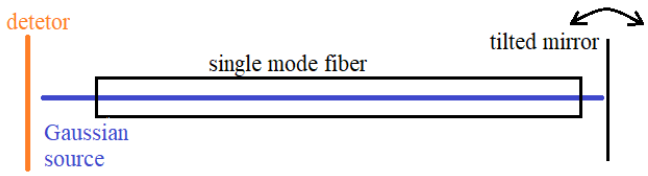

Figure 3.1: Simulation setup of mirror angular misalignment analysis.

The mirror angle is tilted from 0° to 1°. First, I recorded irradiance of perpendicular mirror (0°) to the fiber end-facet. As shown in Fig. 3.2(a), the distribution of output light beam is focused and total output power decreases by 0.7 dB. Second, I tilted the mirror angle to 1° of x-axis. The output distribution is relatively disperse and output power decreases by 5.5 dB. The difference of irradiance indicates that the effect of backward coupling by misaligned mirror is considerable for the proposed FFPI setup.

This simulation I verified in Chapter 5, where the experiments of angular misalignment of ± 6° are carried out. The power decreases about 3 dB per degree, and drops 13 dB in total for 6°. In simulation I also observed power penalty while increasing tilt angle of mirror, as shown in Fig. 3.3. The results shows that even 1° is critical for FFPI, and after incline 4°, most of the power is lost.

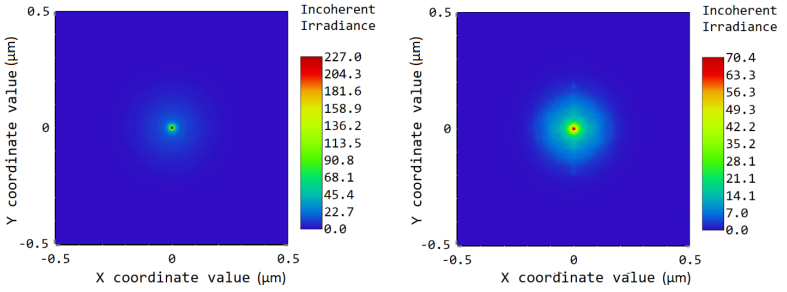

(a) 0° (b) 1°

Figure 3.2: Incoherent irradiance image of (a) 0° and (b) 1° tilted mirror.

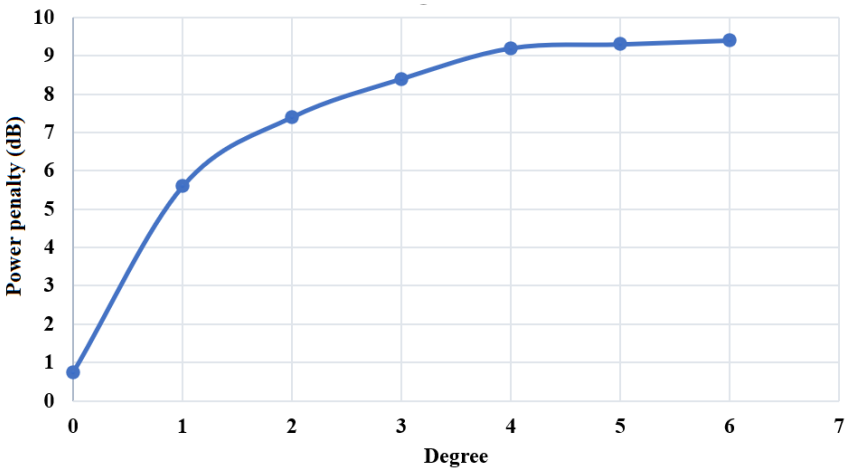

Figure 3.3: Power penalty in dependence on the mirror tilt.

The cross section of irradiance is depicted in Fig. 3.4 and Fig. 3.5, which confirm the power intensity variation as well as the distribution of irradiance. As discussed in Chapter 2.4, backward coupling is affected by angular misalignment and the spatial frequency of transmitted beam components of 1° will have wide distribution than 0°. Moreover, I simulated higher degree of the mirror up to 6° in order to verify the experimental results in Chapter 5. The power drops rapidly in first 4°, then slows down at 5° due to most modes of beam are reflected into the space instead of the fiber. It shows again that an aligned mirror and fiber play a key role in the FFPI performance.

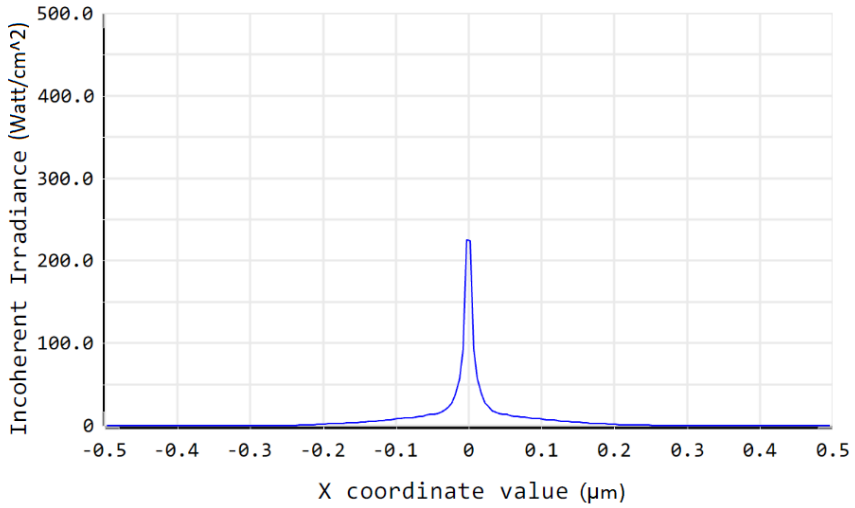

Figure 3.4: Cross section of incoherent irradiance of 0°.

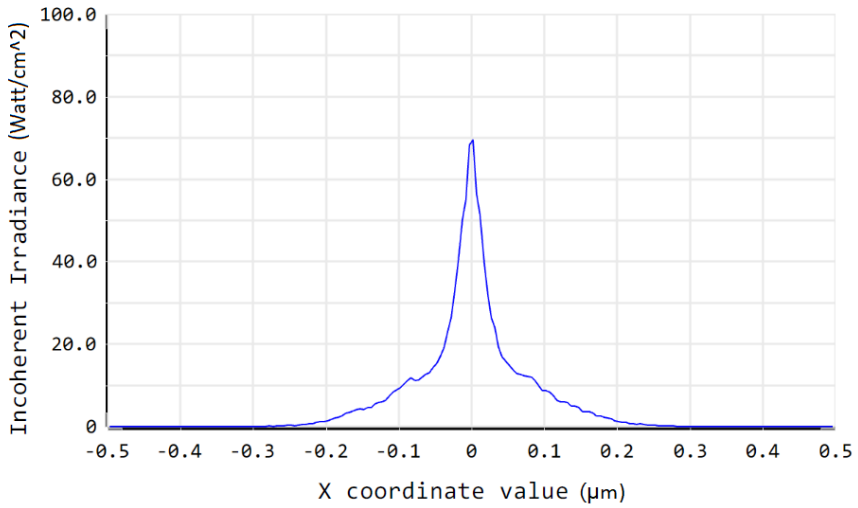

Figure 3.5: Cross section of incoherent irradiance of 1°.

3.2 FPI beam propagation and reflection

In this section a Gaussian beam propagating between the fiber end-facet and the reflective mirror is analyzed. As depicted in Fig. 3.5, an FFPI cavity is formed between a mirror and a silica surface acting as the fiber end-facet. In this case an optical coating at the fiber end-facet is considered. A 10 mW Gaussian coherent source of 1550 nm wavelength generated a collimated beam. The optical coating has the role of back-reflection variation and represents different amount of light reflected back at the fiber end-facet. In order to obtain maximum output power, several additive coatings are tested to achieve total constructive interference as discussed in Chapter 2.2. From simulation results, anti-reflection coating got 2 mW, gold coating has 9 mW reflection and only I.5 coating got 5 mW which is half of input power and it is a necessary condition for total constructive interference. Hence, the FFPI system based on I.5 coating is used for this reflection simulation later on.

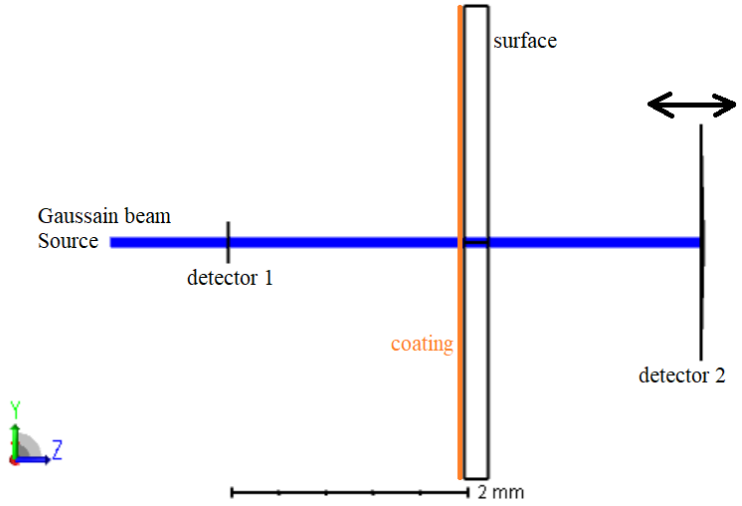

Figure 3.6: Simple scheme for simulating beam propagation and reflection.

The mirror has 100% reflection and detector one tracks output interference pattern generated by back-reflection from the coating and reflected signal from the mirror. The moving mirror is moved from fiber end-facet with a step of 1 μm from 1 μm to 40 mm. The power performances of each moving range are shown in Fig. 3.6. The widest moving range in this simulation has the most stable performance. On the contrary, the sensor is very sensitive with extremely short cavity length since there is no apparent interference pattern. This indicates that when the sensor is detecting with a very short distance in μm scale, it is easily affected by the surrounding environment.

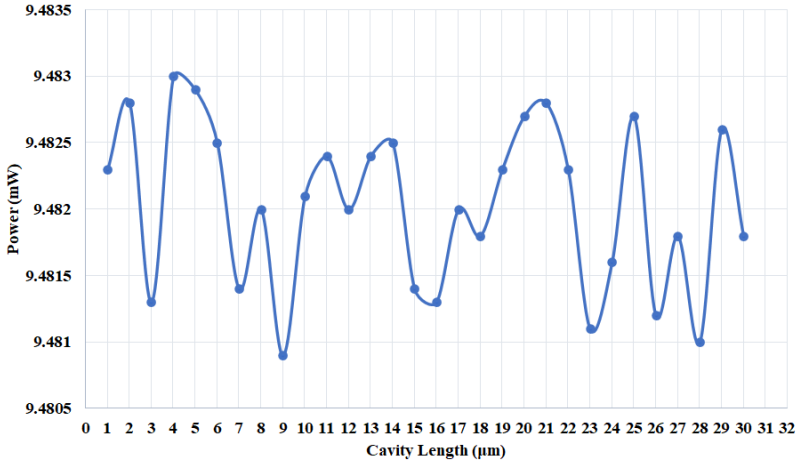

(a) 1 μm-30 μm with step 1 μm

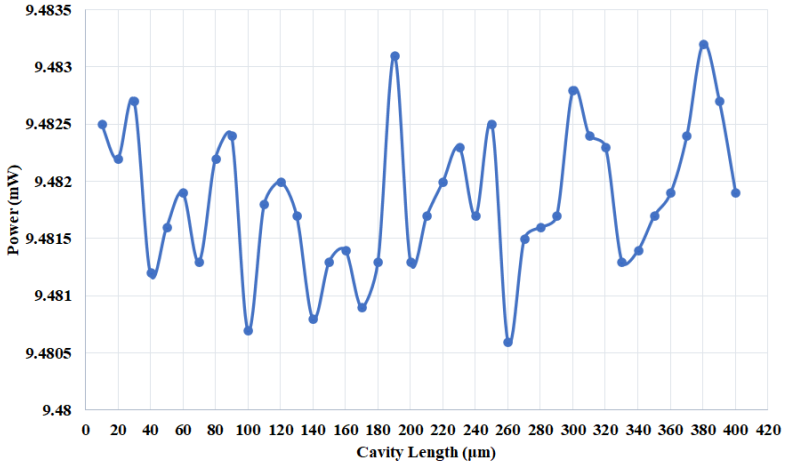

(b) 10 μm-400 μm with step 10 μm

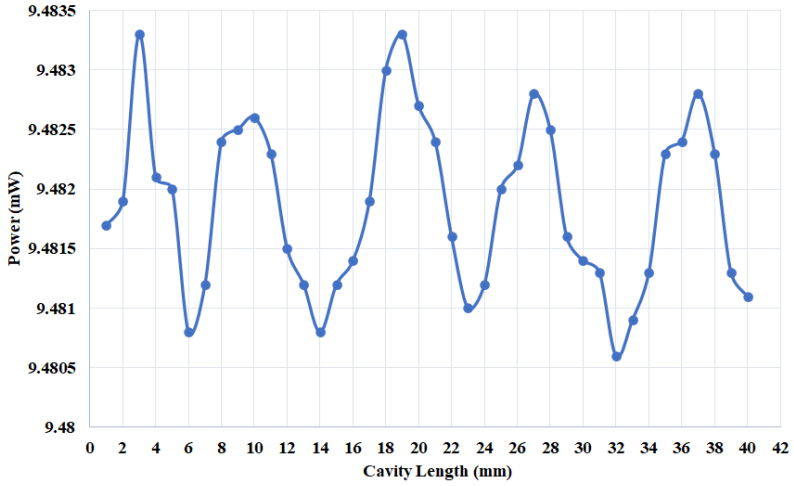

(c) 1 mm-40 mm with step 1 mm

Figure 3.7: Received power in dependence on the cavity length for different mirror ranges, input signal is at 10 mW.

Chapter 4

Experimental setup

4.1 Proposed FFPI configuration

A schematic drawing of the FFPI-based displacement sensor is shown in Fig. 4.1. A stable laser source (LS, CoBrite DX4) at 1550 nm is used as an input light source providing an average optical power of 6 dBm. An optical attenuator (ATT) is included at the laser output to set the required power level for a particular sensing configuration. An optical circulator (CIRC) was placed after ATT. The FFPI cavity is formed between the fiber end-facet and the reflective mirror **M**. The mirror (high-reflectivity mirror with R = 99% or a glass mirror with R = 4%) is mounted on a micromovement 3D stage (NanoMax, MAX313D) with a high resolution of 0.1 voltage piezo, tuned precisely by personal computer (PC). An amplified photodetector (PD) along with an oscilloscope (OSC, LeCroy) is connected to CIRC port 3. For processing, a PC is used, which also controls the voltage step of the piezo controller and processes the interference spectrum simultaneously.

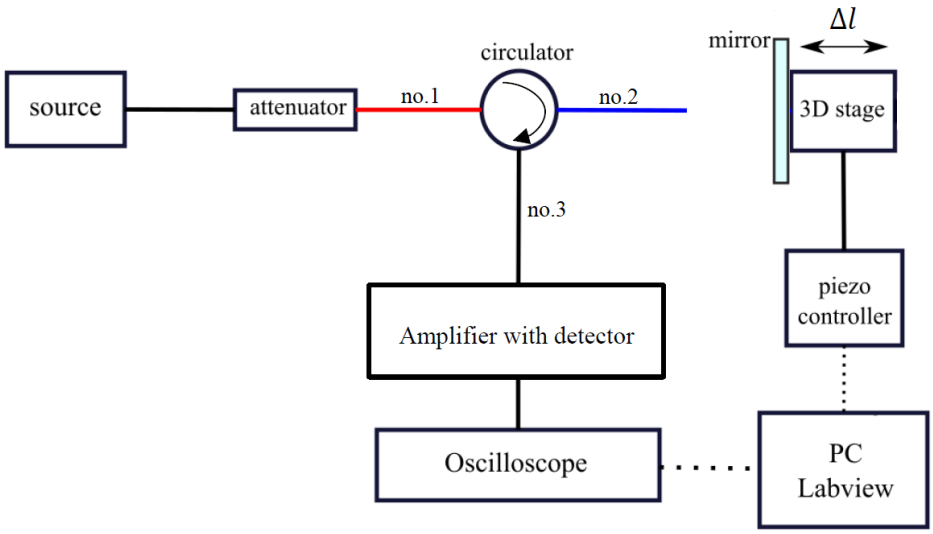

Figure 4.1: Experiment configuration of the proposed FFPI motion sensor.

By moving the mirror, the cavity length is varied. The optical signals are reflected first from the fiber end-facet and then from the mirror. Both reflected signals are then back-coupled into the fiber. Finally, the interference signal shows at the output port. Total constructive interference only occurs when the reflected signal from the mirror has the same amplitude compared to signal reflected from the fiber end-facet. In order to obtain maximum power of interference, the signal reflected from the mirror should ideally have the same intensity as the signal reflected from the fiber end-facet, including the losses caused by back-coupling.

It is required to balance the fiber and mirror arms to the source power, where the sensitivity and modulation depth is the highest.

Two FFPI configuration were analyzed. First (configuration A) with a glass mirror (R = 4%) and a fiber collimator which is a conventional SMF spliced on a 320 μm long segment of graded-index multimode fiber with 100 μm core diameter.

Second (configuration B) with a high-reflectivity mirror (R = 99%) and a single mode fiber (SMF) with physical contact (flat connector).

The PC is connected to OSC using an RJ-45 Ethernet Cable. LabVIEW based data processing program is constructed to obtain standard derivation, peak-to-peak and changing displacement of mirror of FPI motion detection sensor. The experimental setup for resolution of 100 nm of displacement measurements is illustrated in Fig. 4.2.

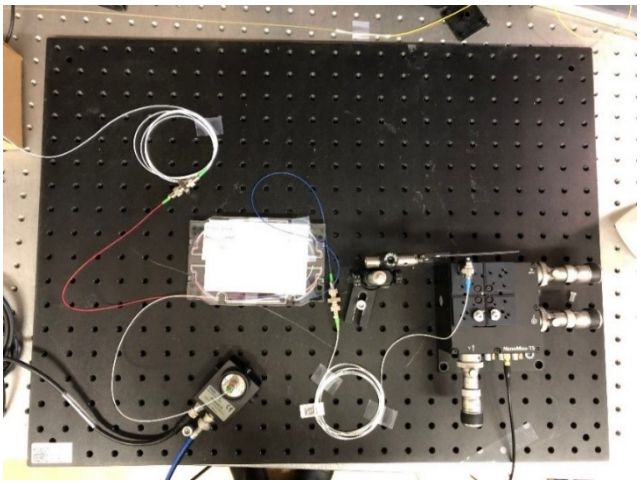

Figure 4.2: A photograph of the experimental setup for FFPI displacement measurement.

4.2 Dual-cavity FFPI configuration

Based on single-cavity FFPI sensor presented in Chapter 4.1, I proposed a dual-cavity FFPI configuration adding a 50:50 fiber coupler and two CIRCs. With 6 dBm average optical power of 1550 nm laser souce, two fiber collimator were connected to each circulator. The amplifier was used depending on the back-reflection from the fiber end-facet. In this configuration, I used the same fiber collimators as in the single-cavity FFPI, as depicted in Fig. 4.3. The rest of setup remain the same with Chapter 4.1, including 3D flexure stage, OSC and piezo controller.

The cavity length of the second FFPI is slightly shifted to enhance the displacement range, as shown in Fig. 4.4. The alignments between mirror and two fibers are still important in the dual-cavity FFPI system. Power meter was used before measurement to detect maximum output power of each FFPI.

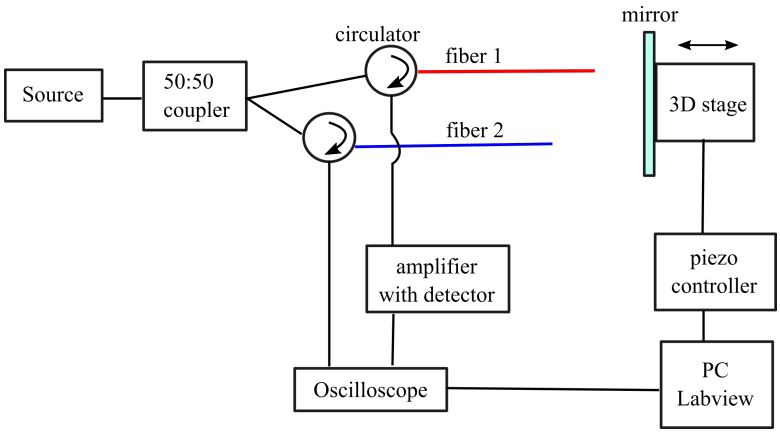

Figure 4.3: Experimental configuration for the dual-cavity FFPI motion detection.

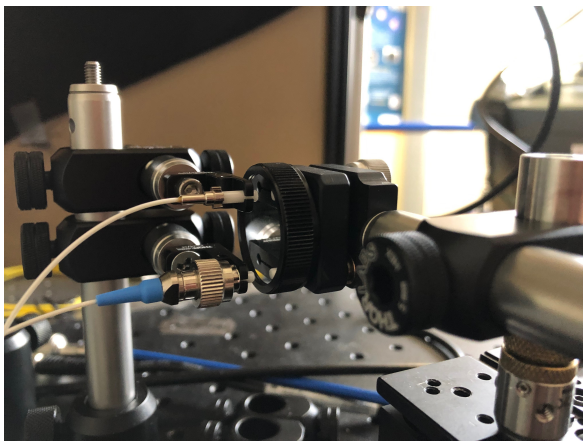

Figure 4.4: Detailed photograph of two cavity lengths of the dual-cavity FFPI displacement measurement.

Chapter 5

Results and Discussion

I first characterized the FFPI sensor using the setup depicted in Fig. 4.1 for the two configurations: configuration A with a 4% reflectivity mirror and a fiber collimator, configuration B with a 99% reflectivity mirror and SMF with a flat end-facet (PC connectors). I power-balanced both configurations and separately analyzed resolution, sensitivity, modulation depth and stability. I also verified the effect of angle misalignment of the mirror by tuning up to 12° from the axis.

For the displacement measurement, I first need the response curve to obtain a calibration. We are able to recalculate displacement by sampling of 0.19 μm/V according to Fig. 5.1. This calibration is important because we can use the value to translate voltage into movement. The working area of the sensor is defined the linear part of the response curve, marked as the red area in Fig. 5.1. A fitting equation is calculated by post-processing for different amplifications of the amplifier from 10 dB up to 40 dB as will be discussed in detail in the next section.

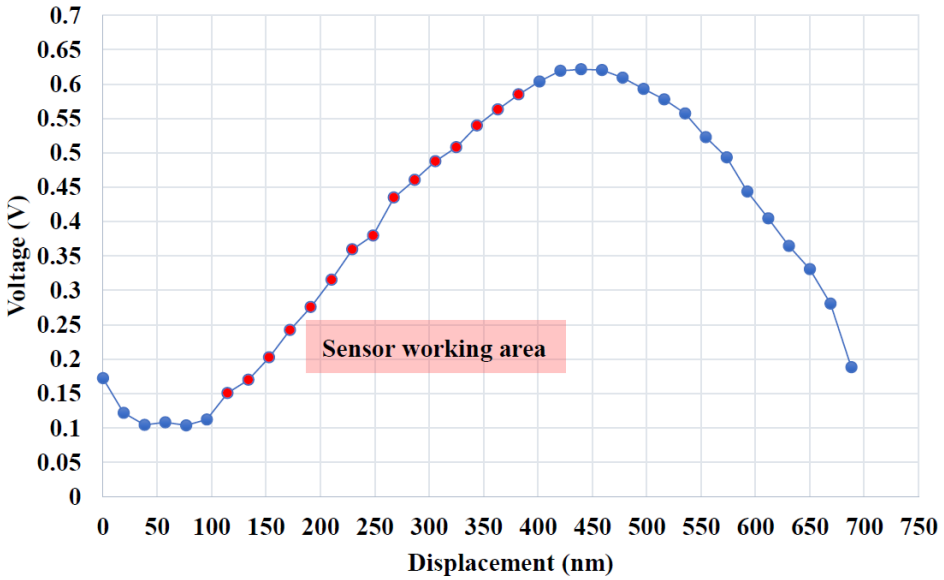

Figure 5.1: Measured voltage in dependence on the mirror displacement (movement).

5.1 Configuration A - 4% mirror with a fiber collimator

In this section, I will discuss experimental results for FFPI configuration A. A linear fitting was first applied to the measured voltage dependence on the mirror displacement, as shown in Fig. 5.2. The value of R^2 is 0.9944, indicating that calculated response and the real displacement have a good linear relationship.

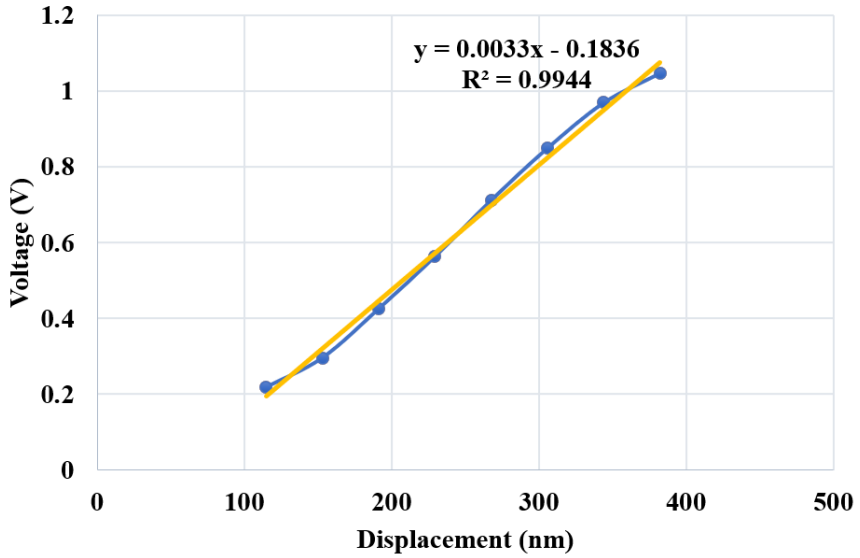

Figure 5.2: FFPI sensor response of movement. Working area and linear fitting of sensor for 40 dB amplification.

I further characterized the FFPI sensor response using a calibration equation of three-order polynomial as:

$$y = -4 \times 10^{-8}x^3 + 3 \times 10^{-5}x^2 - 0.0042x + 0.332 \tag{5.1}$$

along with R^2 of 0.999. This polyinomial function served as calculation of real movement of the FFPI sensor. We will need this relation for future calibration.

Four different amplifications of the detected voltage (corresponding to optical power at the detector) were evaluated and resulted different modulation depth. I tested amplification from 10 dB up to 40 dB. Fig. 5.3 shows that the best outcome provides amplification of 40 dB which means the widest working area of the proposed FFPI displacement sensor.

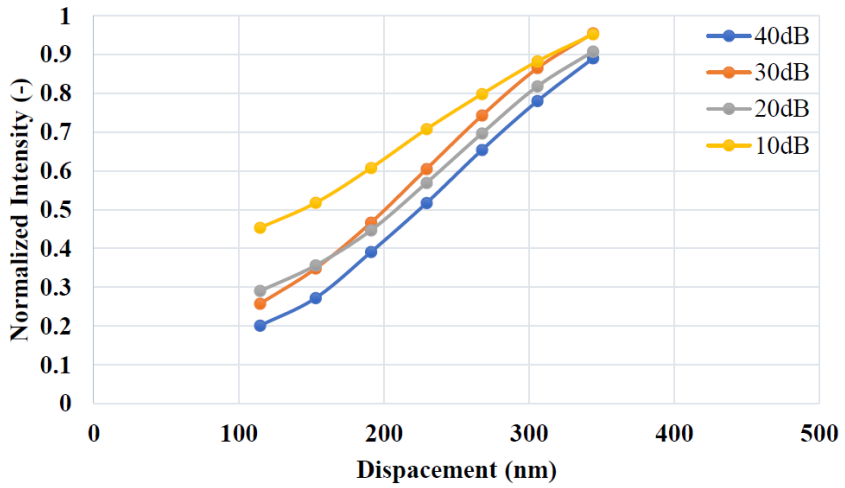

Figure 5.3: Modulation depth of the FFPI sensor for four different amplification levels.

The sensitivity S of the sensor is defined as the ratio of response and measured displacement using the following equation:

$$S = \frac{\Delta V}{\Delta l}, \tag{5.2}$$

where ΔV is the difference of the sensor response, Δl is the corresponding displacement. The sensitivity slope of the transfer function is depicted in Fig. 5.4.

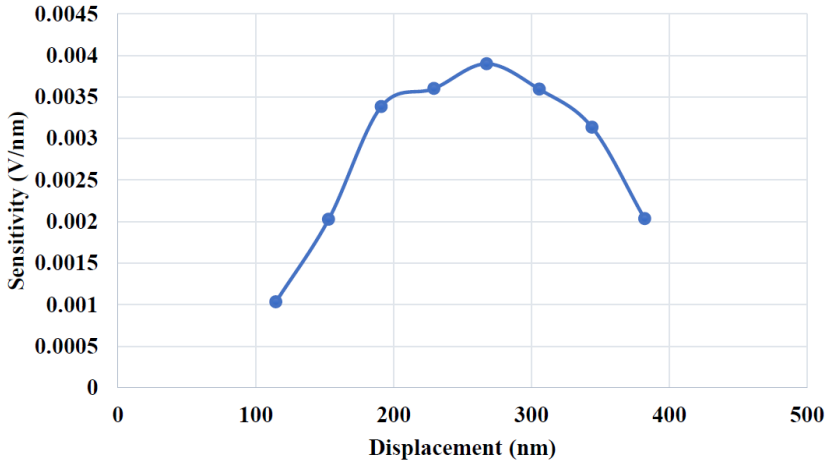

Figure 5.4: Sensitivity of sensor for 40 dB amplification.

In the center of the working area, the sensor has the best sensitivity. This value of 0.004 V/nm indicates how accurate the sensor is. It also proves that a linear working area is required in a good sensor, since sensitivity derived from working area directly affects performance of displacement sensor.

The resolution R is related to the accuracy of the sensor and is then defined as:

$$R = \frac{STD}{S} \tag{5.3}$$

where STD is standard derivation which is also referred as noise in the system. STD is almost a constant value in the sensor working area. Therefore, resolution of FFPI sensor is inversely proportional to the sensitivity. Because the sensitivity has the direct impact from working area, the resolution is also influenced by the performance of working area. The resolution is better than 3 nm in the working area as depicted in Fig. 5.5. The edge of the selected area has resolutions of 4.5 nm and 6.8 nm which are higher than the rest of interval.

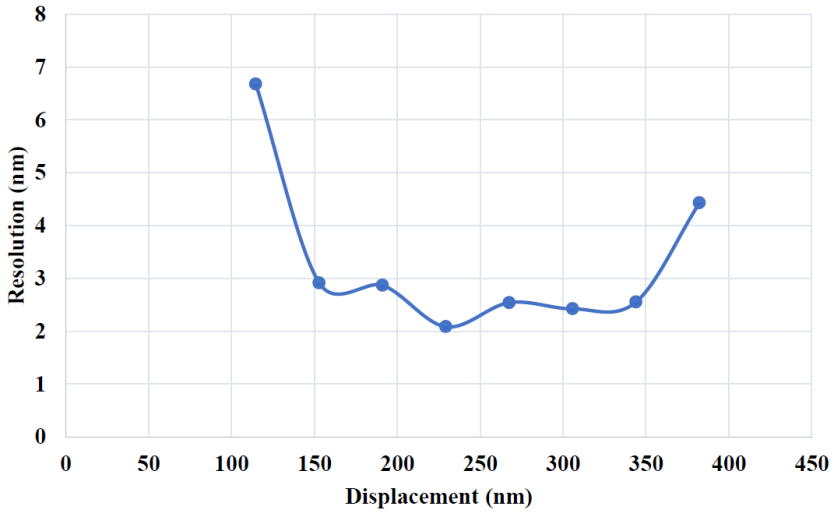

Figure 5.5: Resolution of the FFPI sensor with amplification of 40 dB.

The sensitivity and resolution over a larger displacement area of 1500 nm are shown in Fig. 5.6 and Fig. 5.7. In areas where the resolution exceeds 25 nm, we cannot distinguish which direction of mirror is actually moving. We can not express quality of sensor because of the sensitivity over 10^{-3} V/nm either. Therefore, the FFPI sensor is needed to work in the working area. Fig. 5.6 indicates that in the working areas of each period have higher sensitivity than peaks during measurement. Same situation occurs in Fig. 5.7, best resolution of 2.2 nm is obtained during the interference part referred to working area. Choosing a proper working area of the displacement sensor is obviously an important factor in motion detection. As shown in Fig. 5.8, I applied four amplifications to enhance working area of FFPI sensor.

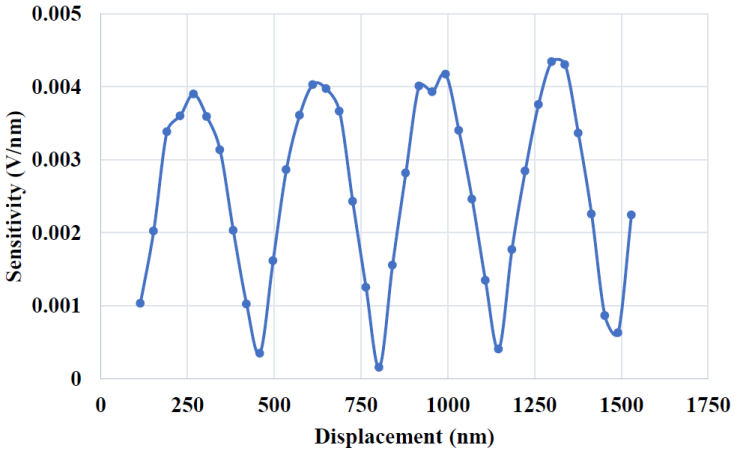

Figure 5.6: Sensitivity over a large area of displacement.

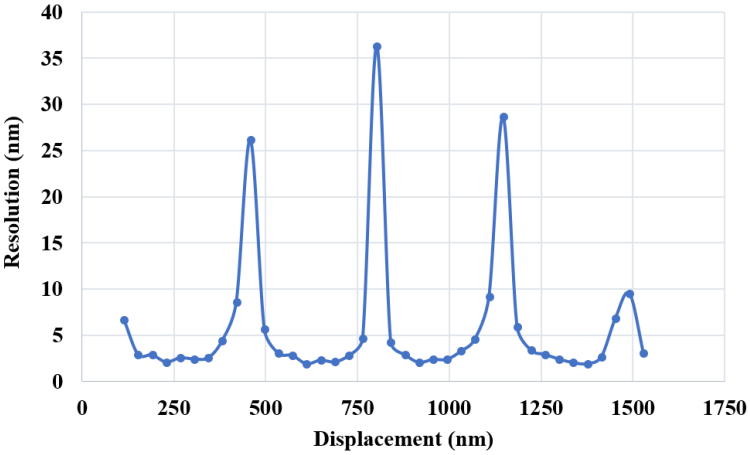

Figure 5.7: Resolution over a large area of displacement.

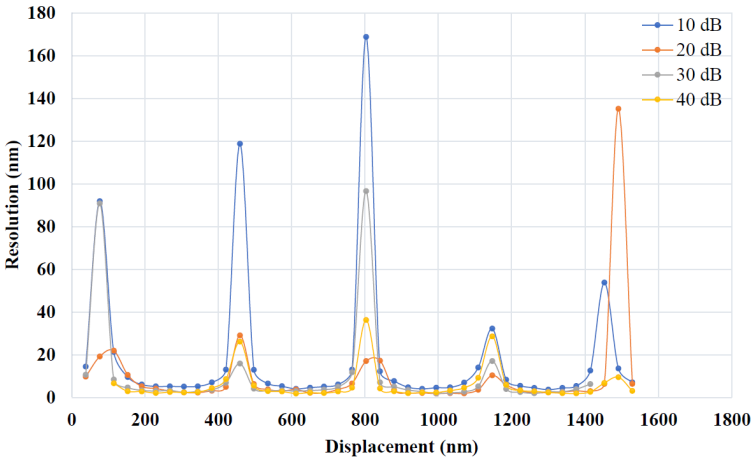

Figure 5.8: Resolution for amplification from 10 dB to 40 dB.

Results from Fig. 5.8 confirm the fact that higher amplification can enhance the resolution and make the sensor performance better even at the edges of the working area. Thanks to the amplification, the sensor can work in a longer distance with a more linear working area.

From analysis of resolution and amplification, we can conclude that using an amplifier to enhance the detected interference signal will enhance the overall performance of the FFPI sensor.

The displacement range is an important parameter in motion detection and represents stability of the sensor. It corresponds to laser coherence length as discussed in Chapter 2.2. As shown in Fig. 5.9, I manually tuned the distance of cavity length by 250 μm step up to 2 mm away from the mirror. I obtained eight sinusoidal interferences which confirm the FFPI sensor stability in this range. It shows perfectly constant period during the measurement. We stopped to measure at 1750 μm away from the glass mirror with R=4% since the coherence length of laser limits the measurable displacement.

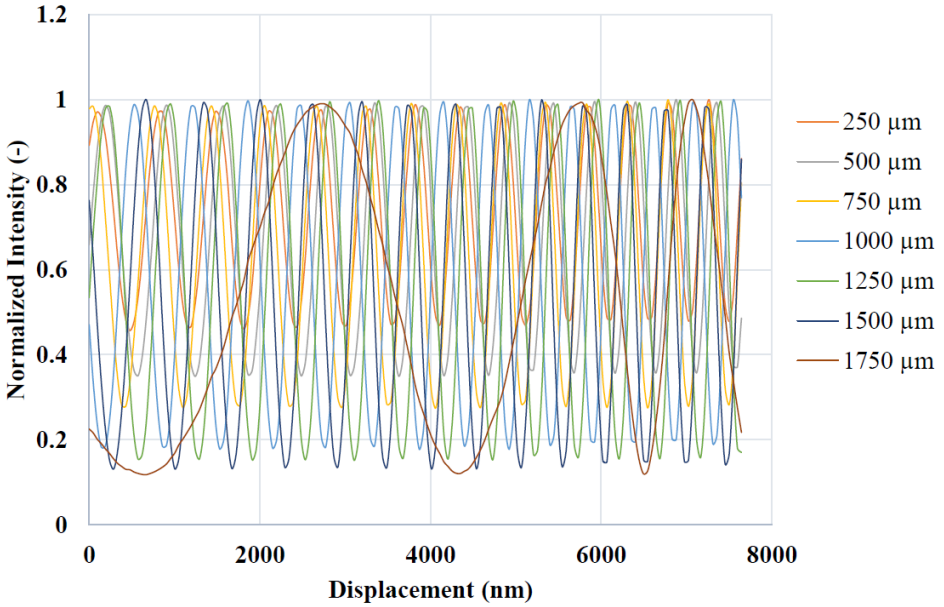

Figure 5.9: Stability of FFPI motion detection with collimated fiber.

Finally, I also tested the effect of angle misalignment of the mirror by tuning ±6 degree on a rotation stage, from the initial position where the back-coupling was the highest. For configuration A, symmetric decreasing power from 0° is observed as shown in Fig. 5.10. The power decreases 3 dB in the first degree, then drops slowly after four degree, indicates that the reflected power is almost lost so output signal approaches zero. It corresponds to the overlap between reflected light and fiber core along with coupling efficiency as mentioned in Chapter 2.3. From this result, we can conclude that the alignment between fiber end-facet and the mirror is critical due to the high loss in small angle change.

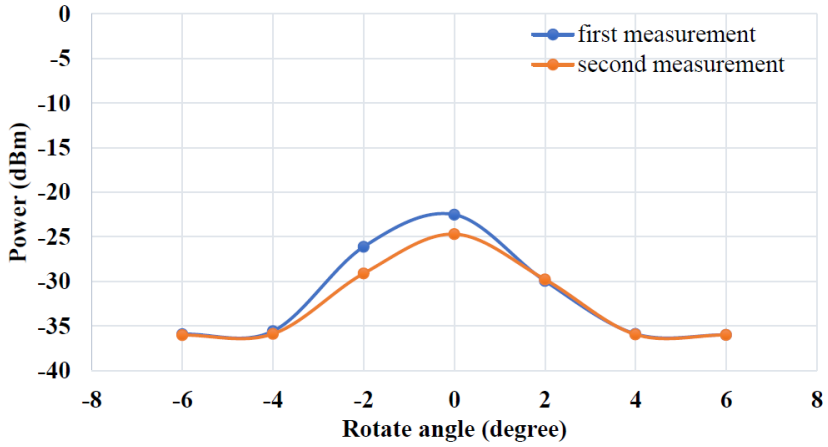

Figure 5.10: Angle misalignment effect of collimated fiber with glass.

5.2 Configuration B - 99% reflection mirror with PC fiber

I used an identical analysis method in Chapter 5.1 for Configuration B - 99% reflection mirror with PC fiber (flat end-facet). In order to obtain same intensity of signal in both arms of FFPI, the cavity is formed between PC fiber and a mirror with 99% reflection. I measured the FFPI sensor response and calculated sensitivity, resolution and standard derivation, respectively.

I obtained sensitivity of 0.02 V/nm from Eq. 5.2 and resolution of 2.36 nm from Eq. 5.3. Compared to sensitivity of 0.004 V/nm and resolution of 2.08 nm of configuration A, performance of configuration B is affected by non-collimated beam propagation in the FFPI cavity.

A linear equation is fitted with sensor response to show the dependence between sensor response and displacement, as shown in Fig. 5.11. The working area with R^2=0.99 still acts well near the center point. Therefore, we can expect that the performances of configuration B is good enough for motion detection.

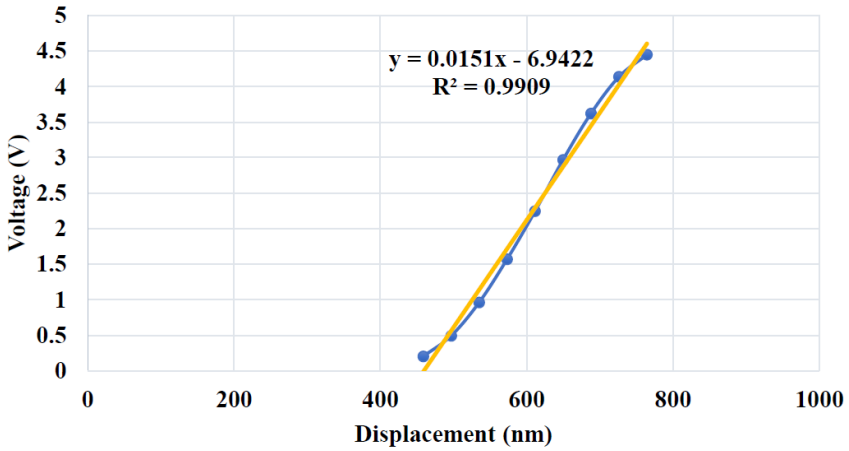

Figure 5.11: Sensor response of standard single mode fiber.

The sensor response is calibrated and characterized again with three orders of polynomial equation by:

$$y = -2 \times 10^{-7}x^3 + 4 \times 10^{-4}x^2 - 0.2087x + 37.613 \tag{5.4}$$

with R^2 of 1 for 40 dB amplification. This equation is served as future calibration and provides relationship between voltage response and real movement.

The working area, modulation depth, sensitivity and resolution are showed in Fig. 5.12. We can improve the FFPI sensor again by amplifying signal. We can solve the divergence effect by selecting narrower working area by reducing 10% range, but at the same time the practicality of sensor will decrease.

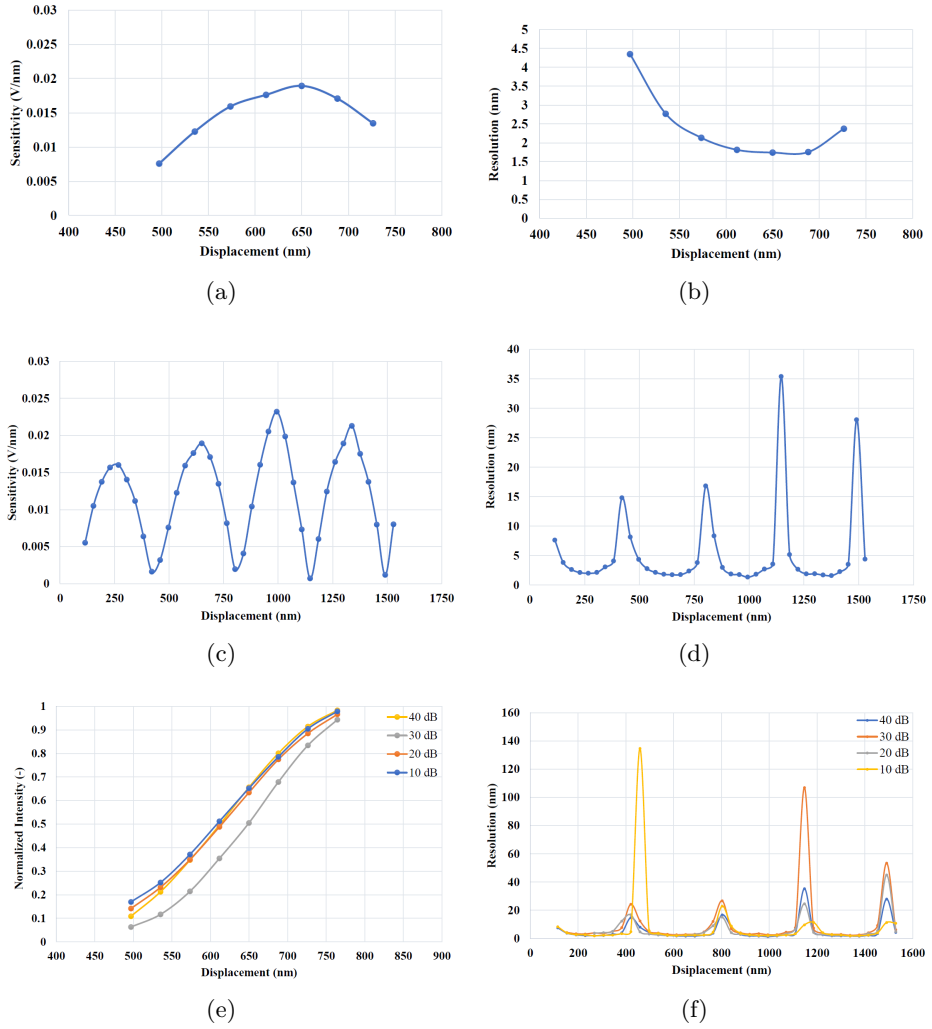

Figure 5.12: (a) Sensitivity, (b) resolution for 40 dB amplification of PC fiber with mirror measurement; (c) sensitivity and (d) resolution for scanning large area; (e) modulation depth of sensor with four different amplification and (e) resolution of four amplifications.

Stability of configuration B is shown in Fig. 5.13. I tuned the cavity length by 250 μm step from 2 mm down to 750 μm. I stopped to measure at 750 μm away from 99% reflection mirror because of limitation by the coherence length of laser. FFPI cavity between PC fiber and the mirror still performed good stability during measurement because of the constant periods. This indicates that the experimental setup based on FFPI is suitable for motion detection. We only need to focus on the proper arms for balanced power and collimated beam propagation in the cavity. Since the coupling and overlapping at the fiber core is weaker than fiber collimator, the movement range of 1250 μm is shorter than 1750 μm of configuration A.

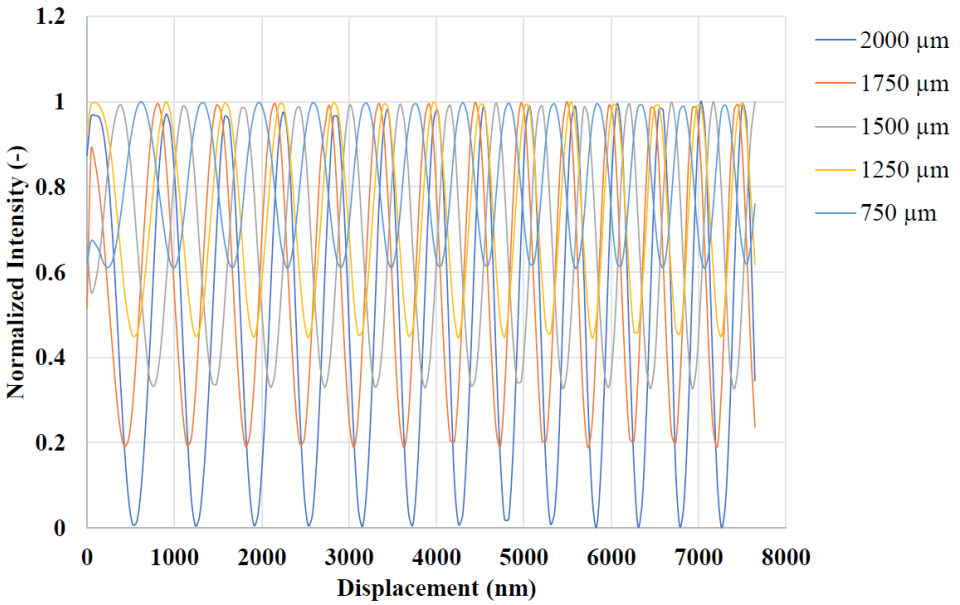

Figure 5.13: Stability of displacement sensor of PC fiber with mirror.

To test the effect of mirror angular misalignment for configuration B, the measurement were done by tilting ±6 degree on the ratation stage. I measured two times to show repeatability of sensor system as shown in Fig. 5.14. The power decreased 1 dB per degree misalignment. Then it slows down at four degree. The symmetric power decreasing indicated again that the perpendicular mirror to fiber end is necessary and critical in FFPI detection.

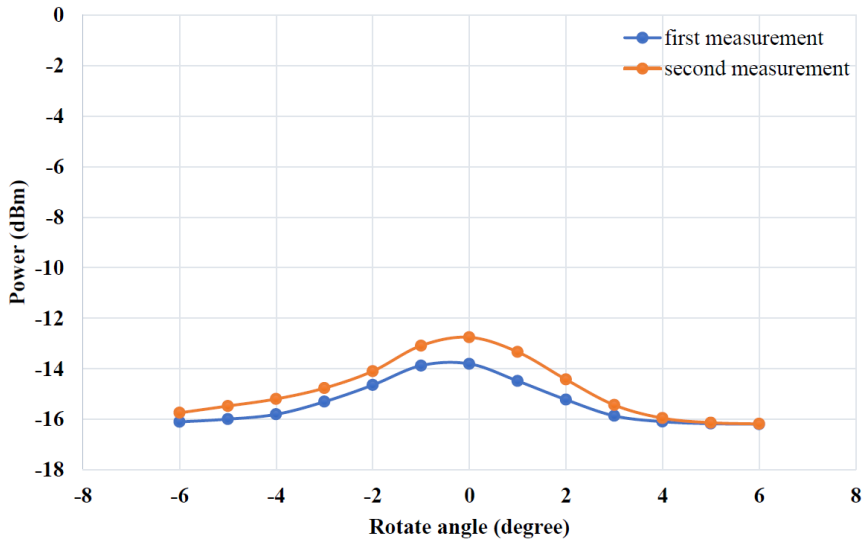

Figure 5.14: Angle misalignment effect of PC fiber and mirror.

5.3 Evaluation of the FFPI sensor using a random signal

To truly analyze the proposed FFPI sensor performance, I have prepared a calibration signal and a random motion signal. The calibration signal was moving the mirror via the piezo controller of 0.1 V step. The random motion signal was manually moving the mirror by the micromovement 3D stage.

I need to calibrate the signal first before evaluate the random signal. The voltage signal from the piezo controller was treated as the reference data set. The corresponding measured voltage signal from OSC (the measured interference) was used for calibration. I fitted the working area of the motion signal with a polynomial function, as shown in Fig. 5.15.

Then I converted both voltages from the reference data set and measured data into displacement, referring to fitting and reference results respectively. I presented the resulting dependencies in Fig. 5.16, comparing measured with reference results. High level of correlation can be observed showing great performance of the proposed FFPI sensor.

Using fitting and reference results shown in Fig. 5.16, I investigated the optical signal's own average error. Average error of 7.58 nm and 0.11 nm at the center of working area were achieved, respectively. These errors are caused by sensitivity limitation, background noise and artificial setup, which is clearly shown by the deviation in Fig. 5.16 and Fig. 5.17.

Finally, I evaluated the random signal which is observed by manually moving the mirror. I verified and analyzed FFPI sensor performance by the fitting result from calibration. The error of the sensor at 1550 nm is showed by comparison of real random motion and analysis signal in Fig. 5.17. These results indicate that the sensor works well by our post-processing and will be a outlook for more complex motion sensor based on FFPI.

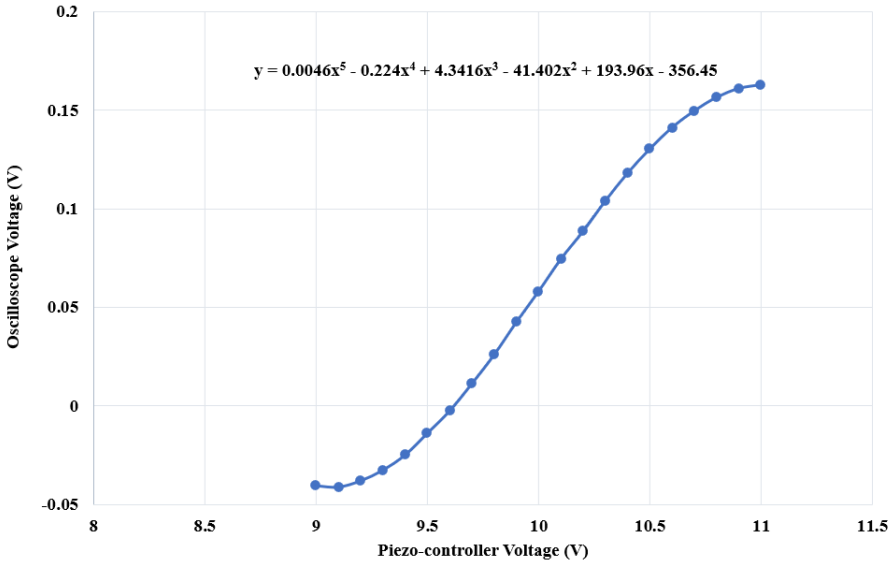

Figure 5.15: Calibration of sensor by fitting function.

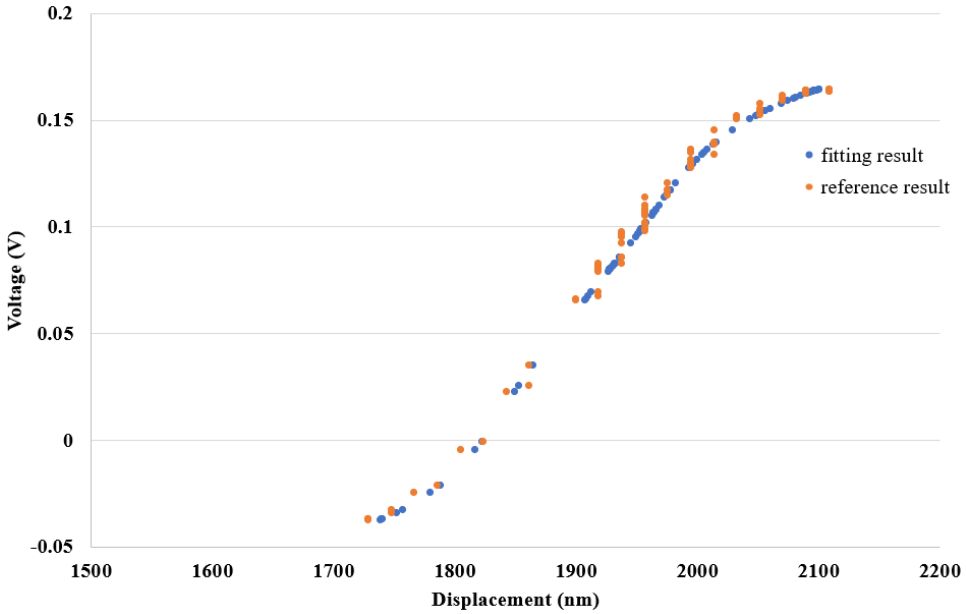

Figure 5.16: Deviation of sensor.

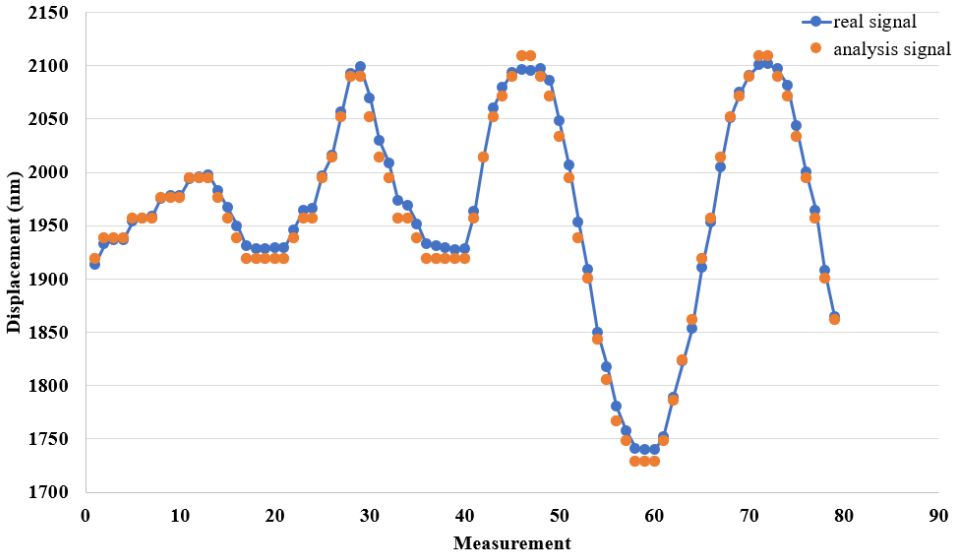

Figure 5.17: A random signal with analysis result.

5.4 Dual-cavity FFPI performance

Dual-cavity FFPI is presented in this section to enhance performance for motion detection and prove the concept in Chapter 5.1 to 5.3. Dual-cavity FFPI is an enhanced type of the FFPI sensor I presented before. The basic principle is using two working areas with different cavity lengths. The length difference causes a shifted phase between the propagating signals. The sensitivity area (working area) of one FFPI are used for dual-cavity FFPI sensor. The rest of less sensitive area are always derived from the working area of second FFPI. Because non-woking area is benefit from other, we can precisely measure movement even at the peak of the signal. This replacement of working area achieved wider displacement range for FFPI sensor.

In this section, I first measured the dual-cavity FFPI at 1550 nm to relate to the previous experiments. Second, I verified period difference between 1550 nm and 1310 nm. I was able to reach a wider working area with same post-processing method used in Chapter 5.1 and 5.2.

Two fiber collimators with same 1550 nm laser source were measured in a short period to show their working area respectively. The wider working area is achieved by benefiting from the other's shifted one. As shown in Fig. 5.18, we can define the low sensitivity region out of green working area of fiber one by red working area of fiber two. This solves the working limitation of single FFPI sensor, we can describe quality of whole interference pattern with high resolution and good sensitivity.

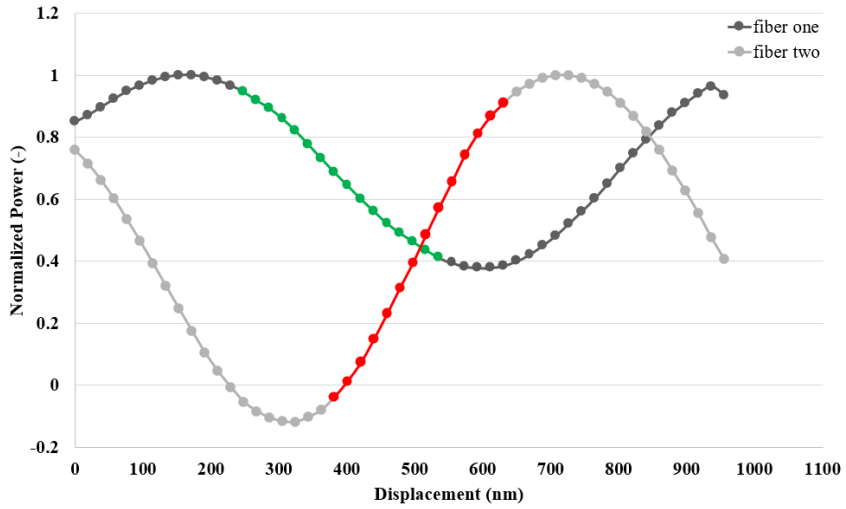

Figure 5.18: Dual FFPI motion detection at 1550 nm.

We can measure motion detection in a wide range of movement, as shown in Fig. 5.19. The sensor performance is stable which verifies the simulation in Chapter 3.2. This overcomes the limited sensing range defect of FFPI sensor. We can have good sensitivity and resolution over a large area continuously without interruption, which is an important aspect of a high-quality displacement sensor.

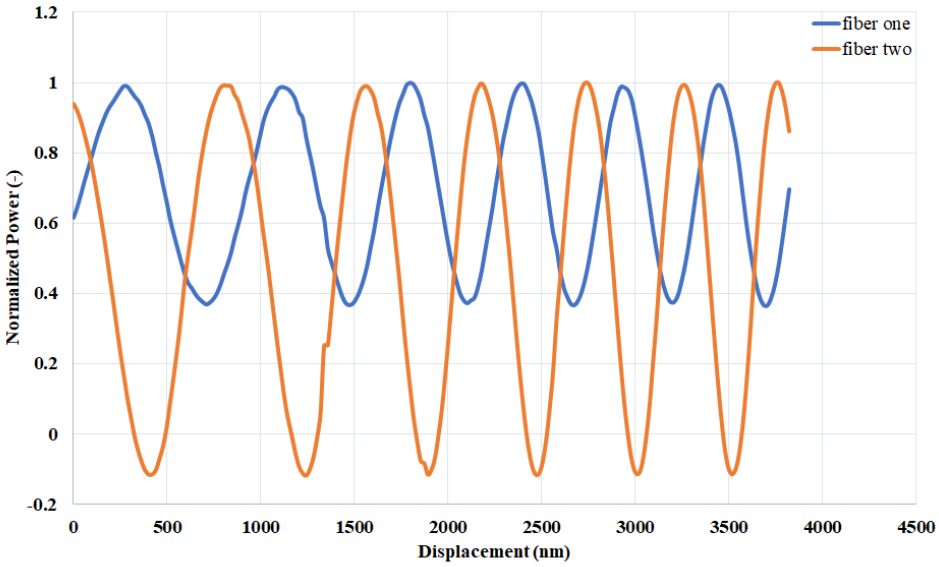

Figure 5.19: Dual FFPI motion sensor in a wide range measurement.

Finally I tested the dual-cavity FFPI for two different wavelengths of the laser source. The period of observed interference pattern was shifteed in relation to the wavelength of the laser source. Figures 5.20 and 5.21 depict the measured dependencies with interference period of 611 nm and 764 nm respectively.

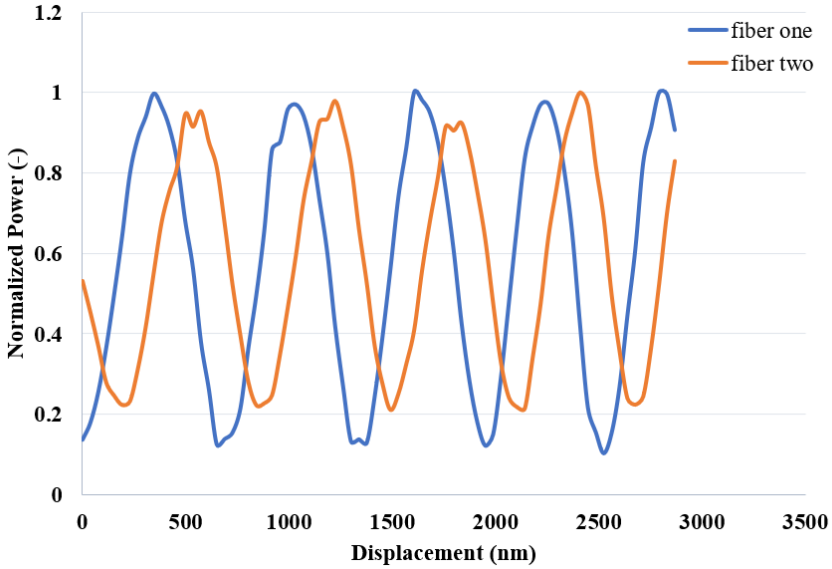

Figure 5.20: Dual-cavity FFPI displacement sensor with 1310 nm wavelength.

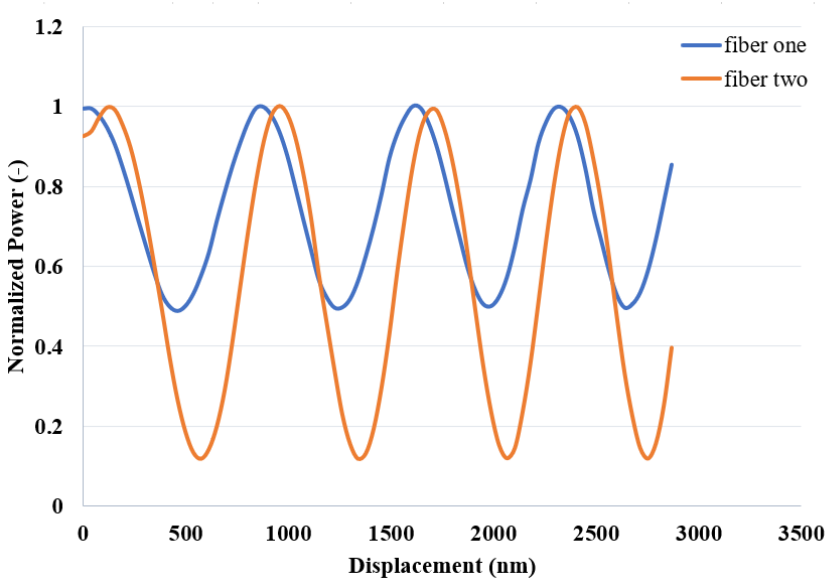

Figure 5.21: Dual-cavity FFPI displacement sensor with 1550 nm wavelength.

Chapter 6

Conclusion

I proposed, designed, simulated, constructed and experimentally verified highly-sensitive motion detection based on the fiber Fabry-Perot interferometer. The FFPI cavity was formed between a fiber end-facet and a discrete moving reflective mirror. A fiber collimator was exploited to enhance the backward coupling efficiency. Dual-cavity FFPI was proposed to enhance the sensor measurement range.

The calibration of the FFPI sensor was first derived from the sensor response curve and served as a translation between measured voltage (in terms of detected optical signal) and mirror displacement. The working area of the FFPI sensor was approximated with a linear fit.

I presented two configurations (a 4% reflection mirror and 99% reflection mirror with fiber collimator and single mode fiber, respectively). Displacement range up to 1500 μm and resolution of 2.08 nm was obtained.

Angular offset effect on the backward coupling was evaluated and verified in measurement. The power drops 3 dB when there is an 1° misalignment. For comparison, I obtained resolution of 2.36 nm due to non-collimated beam propagation.

I evaluated average movement error of sensor which is 7.58 nm between real and reference signals while the minimum error of 0.11 nm occurs at the center of working area.

The stability of sensor was verified by scanning a large area up to 4 mm. The low-cost, simple and robust system with sub-micrometer resolution can be easily commercialized and has great potential for applications in the industry requiring extremely precise displacement measurement.

Bibliography

[1] Seat, Han Cheng, and Saroj Pullteap. "An extrinsic fiber Fabry-Perot interferometer for dynamic displacement measurement." IEEE International Conference on Mechatronics and Automation, Aug., 2007.

[2] Chen Zhu, Yizheng Chen, Yang Du, Yiyang Zhuang, Fengxue Liu, Rex E. Gerald, II, and Jie Huang, "A displacement sensor with centimeter dynamic range and submicrometer resolution based on an optical interferometer." IEEE Sensors Journal vol.17, no.7, pp. 5523-5528, Sep., 2017.

[3] S. Khaliq, S. W. James, and R. P. Tatam, "Fiber-optic liquid-level sensor using a long-period grating," Opt. Lett., vol. 26, no. 16, pp. 1224–1226, Aug. 2001.

[4] B. Yun, N. Chen, and Y. Cui, "Highly sensitive liquid-level sensor based on etched fiber Bragg grating," IEEE Photon. Technol. Lett., vol. 19, no. 21, pp. 1747–1749, Nov., 2007.

[5] B. Yun, N. Chen, and Y. Cui, "Highly sensitive liquid-level sensor based on etched fiber Bragg grating," IEEE Photon. Technol. Lett., vol. 19, no. 21, pp. 1747–1749, Nov., 2007.

[6] V. Bhatia and A. M. Vengsarkar, "Optical fiber long-period grating sensors," Opt. Lett., vol. 21, no. 9, pp. 692–694, May, 1996.

[7] J. P. Chen, J. Zhou, and Z. H. Jia, "High-sensitivity displacement sensor based on a bent fiber Mach–Zehnder interferometer," IEEE Photon. Technol. Lett., vol. 25, no. 23, pp. 2354–2357, Dec., 2013.

[8] Qiangzhou Rong, Xueguang Qiao, Yanying Du, Dingyi Feng, Ruohui Wang, Yue Ma, Hao Sun, Manli Hu, and Zhongyao Feng, "In-fiber quasi-Michelson interferometer with a core– cladding-mode fiber end-face mirror," Appl. Opt., vol. 52, no. 7, pp. 1441–1447, Mar., 2013.

[9] Yanjun Li, Wenqi Wu, "Research on Physical Parameter Measurement System of Fiber Fabry-Perot Interferometer", IEEE International Conference on Manipulation, Manufacturing and Measurement on the Nanoscale, Aug., 2018.

[10] KTV Grattan, T Sun, “Fiber optic sensor technology: an overview”, Sensors & Actuators A Physical, vol. 82(1), pp. 40-61, 2000.

[11] D Stacey, “The Fabry-Perot Interferometer. History, Theory, Practice and Applications”, Optics Lasers in Engineering, vol. 37(7), pp. 1279-1280, 1991.

[12] MJ Gander, WN Macpherson, JS Barton, RL Reuben, JDC Jones. et al., “Embedded micromachined fiber-optic Fabry-Perot pressure sensors in aerodynamics applications”, IEEE Sensors Journal, Vol. 3 (1), pp. 102-107, 2003.

[13] Optics fifth edition, Eugene Hecht, Person Education Limited, © 2017. [cit. 5. 5. 2020].

[14] Tutorial: Fiber Optic Basics, In: Newport Corporation. [online]. Newport Corporation, © 2020. [cit. 2. 2. 2020]. Available: https://www.newport.com/t/fiber-optic-basics

[15] R. Paschotta, article on ’fiber collimators’ in the Encyclopedia of Laser Physics and Technology, 1. edition October 2008, Wiley-VCH, © 2020. [cit. 2. 2. 2020]. Available: https://www.rp-photonics.com/fiber_collimators.html

[16] Jae Yong Lee, Jae Won Hahn, and Hai-Woong Lee, “Spatiospectral transmission of a plane-mirror Fabry-Perot interferometer with nonuniform finite-size diffraction beam illuminations”, Journal of the Optical Society of America. A, vol. 19, no.5, pp. 973-984, 2002.

[17] Fiber optic measurement techniques, Rongqin Hui and Maurice O’Suliivan, Elsevier Inc., © 2009. [cit. 2. 5. 2020].

[18] Ali, Adnan Hussein, Sahib N. Abdul–Wahid, and Hussein A. Mohammed. "Analysis of Laser Linewidth Measurements Based on Fabry Perot Interferometer System." IJECS., vol.3838, no.60, pp.1223, 2013.